Key Points:
- First detailed study of small-scale (<10 km) magnetic fluctuations at mid- and low-latitudes which are interpreted as narrow, intense FAC
- Events show distinct occurrence rate distributions in different frames; there are two groups of events, morning-noon and evening-night
- The similar distribution features of small-scale events with medium-scale TIDs suggest a close relation between the two phenomena

Correspondence to:
F. Yin,
yinfan@whu.edu.cn

Comprehensive Analysis of the Magnetic Signatures of Small-Scale Traveling Ionospheric Disturbances, as Observed by Swarm

Fan Yin[1], Hermann Lühr[2], Jaeheung Park[3,4], and Ling Wang[1]

[1]Department of Space Physics, Electronic Information School, Wuhan University, Wuhan, People's Republic of China, [2]Sect. 2.3, Geomagnetism, GFZ-German Research Centre for Geosciences, Potsdam, Germany, [3]Korea Astronomy and Space Science Institute, Daejeon, South Korea, [4]Department of Astronomy and Space Science, University of Science and Technology, Daejeon, Korea

Abstract Based on Swarm satellite data from 2015 through 2018, we present the mean characteristics of magnetic field fluctuations at midlatitudes and low latitudes. It is the first comprehensive study focusing on small-scale variations (<10 km). Events are observed on about 35% of the orbits. The highest occurrence rates are detected after sunset, in the East Asian/Australian sector, and during months around June solstice. Low occurrence rates are found at low magnetic latitudes (below $\pm 10°$ quasi-dipole latitude), in the region of the South Atlantic Anomaly, and during equinox seasons. All these occurrence features compare well with those of medium-scale traveling ionospheric disturbances. We therefore term our small-scale events small-scale traveling ionospheric disturbances (SSTIDs). SSTIDs exhibit high field-aligned current (FAC) densities connected to narrow current sheets with meridional width of typically 4 km. The intense FACs of several $\mu A/m^2$ flow typically between the hemispheres. Return currents are distributed over larger scales and thus have smaller amplitudes. Peak current densities get larger toward lower latitudes. There are two groups of events, around morning-noontime and evening-night, which are separated by demarcation lines near 04 and 15 magnetic local time. The magnetic amplitudes of the small-scale fluctuations are larger in sunlight than in darkness, indicating larger total currents in the loops. But the FAC peak current densities are larger in darkness, inferring a stronger squeezing of the current sheet under low-conductivity conditions. We suggest that our SSTIDs are an evolutional state of medium-scale traveling ionospheric disturbances.

1. Introduction

Traveling ionospheric disturbance (TID) is a typical ionospheric disturbance phenomenon at midlatitudes and is divided into large-scale (period longer than about 60 min and horizontal wavelengths exceeding 1,000 km) and medium-scale or mesoscale (periods between about 15 min and an hour, wavelengths of several hundred kilometers). Large-scale TIDs tend to travel from high latitudes to the equator, and the source is believed to be auroral or geomagnetic activity at high latitudes. According to Tsugawa et al. (2007, Table 1) the sources of medium-scale TIDs (MSTIDs) are different for different local time sectors. Nighttime MSTIDs are generated by synergistic effects of sporadic *E* and Perkins instabilities (Yokoyama et al., 2009), while the daytime MSTIDs are believed to be directly driven by neutral atmospheric perturbations. Previous statistical analyses of TIDs have been mainly based on ground-based facilities, such as all-sky airglow cameras (e.g., Huang et al., 2016; Shiokawa et al., 2003) and global positioning system (GPS) networks (Chen et al., 2019; Otsuka et al., 2013; Yu et al., 2016). As the oceanic areas lack ground-based facilities, only a few papers, which made use of in situ plasma density data from low-Earth-orbit satellites, could deal with global climatology of TIDs (e.g., Kil & Paxton, 2017).

MSTIDs are accompanied by electric field fluctuation (midlatitude electric fluctuations: MEF) and magnetic field fluctuation (midlatitude magnetic fluctuations: MMF) (Yokoyama & Stolle, 2016). Saito et al. (1998) used Freja satellite and MU radar (the Middle and Upper Atmosphere Radar) radar data to study the mechanism of MEF generation. They found that the MEF event detected by Freja was identified at the same time as MSTID nighttime event. This relation was further confirmed by Shiokawa et al. (2003) using more ground-based and satellite observations. Park, Lühr, Stolle, Rother, Min, Chung, et al. (2009) investigated the magnetic fluctuations caused by midlatitude MSTID. Based on the close relationship between MEF, MMF, and MSTID, one can construct a global climatology of the field fluctuations and use it as a proxy

for MSTID statistics. For example, Saito et al. (1995) were the first to present the initial global statistic of MEFs based on Dynamic Explorer-2 satellite data. The MEF occurrence rate was high during nighttime and at midlatitudes (20–50° invariant latitudes). Park, Lühr, Stolle, Rother, Min, Chung, et al. (2009) presented the nighttime MMF climatology extracted from magnetic field data of the Challenging Mini-Satellite Payload satellite. The nighttime MMFs were more frequent during solstice seasons than in equinoxes, and a global minimum existed near the South Atlantic Anomaly (SAA) of the geomagnetic field. The nighttime MMF occurrence rate tends to move poleward as time elapses from the sunset. On the other hand, Nakanishi et al. (2014) focused on daytime medium-scale magnetic fluctuations, as observed by Challenging Mini-Satellite Payload, which show a climatology different from that of nighttime MMFs. The daytime fluctuations have larger amplitudes than the nighttime MMFs, and the seasonal variation exhibits a main peak during June solstice. Furthermore, there are two hot spots in their global activity distribution, a main peak in the American/Atlantic sector and a weaker one near East Asia/Oceania. The typical features of daytime fluctuations are confirmed further by Swarm observations (Aoyama et al., 2017). These dayside magnetic fluctuations have not been related to MSTIDs.

It has to be noted that all the above-mentioned statistical studies on MMFs were based on satellite magnetic field data averaged over 1 s; hence, the Nyquist frequency (highest frequency that can be resolved) is 0.5 Hz, which corresponds to an along-track wavelength of about 15 km. Although the MEF study by Saito et al. (1995) made use of 16 Hz E field data, the overall statistics was dominated by the larger-scale (several to tens of seconds) fluctuations. Saito et al. (1995) did not describe explicitly the filter used for the statistics. Anyhow, the filter cutoff period used for their examples in the figures was longer than 7 s (i.e., including wavelengths of at least 50 km), and the example spectra in Saito et al. (1995, Figure 6) show only weak signals for frequencies above 2 Hz. Hence, all the previous studies on the MEF and MMF put emphasis on medium-scale features, which correspond to along-track wavelengths of more than 15 km.

So far MMFs of small-scale sizes (along-track wavelengths of 300 m to 7.5 km; corresponding to 1–25 Hz) in the ionosphere are not well studied. It is probably due to the lack of high-precision and high-sampling observations of magnetic fields. This is the first study of small-scale MMFs at F layer altitudes. Thanks to the good quality of Swarm magnetic data at 50 Hz data rate, it is possible to close that gap. Our data set from all three Swarm satellites, covering 4 years (2015–2018), enables us to investigate the details of the small-scale events. Specifically, we can deduce the relation of small-scale MMF climatology to that of medium-scale MMFs and MSTIDs as reported in previous studies.

In section 2 we briefly introduce the used instruments and data processing methods. Section 3 presents some examples, and section 4 describes the statistics of small-scale MMFs, which will be thoroughly discussed and compared with previous studies in section 5. Finally, new findings are summarized, and conclusions are drawn in section 6. Note that in the following sections we use the terms MMF and MSTID interchangeably and name the small-scale MMFs, of interest here, commonly small-scale traveling ionospheric disturbance (SSTID).

2. Instruments and Data Processing Methods

2.1. Swarm Mission

The constellation mission Swarm is one of ESA's (European Space Agency) Earth Explorers. The major objective of this space mission is to fully investigate the Earth's magnetic field with the most advanced survey. The mission consists of three identical satellites labeled Alpha, Bravo, and Charlie (A, B, and C), which were launched on 22 November 2013 into a near-polar orbit. The final constellation of the mission was achieved on 17 April 2014. Swarm A and C form the lower pair of satellites, flying side by side (separated east-west by about 1.4° in longitude and about 50 km in north-south) at an altitude of 462 km (initial altitude) and at 87.35° inclination angle, whereas Swarm B is cruising at a higher orbit of 511 km (initial altitude) and at 87.75° inclination angle. Due to the different inclination angles and altitudes, the ascending node of Swarm-B separates gradually from those of the other two satellites (A/C pair). In 2018 the orbital plane of Swarm B is perpendicular to the lower A/C pair. The LTAN (local time of the ascending node) repeats after about 267 days for the Swarm A/C pair, and it takes about 280 days for Swarm B. The deployment of a constellation can provide multipoint measurements on global and regional scales and provides more information about the spatial and temporal variations of the signals than a single satellite.

Each Swarm satellite carries the same scientific payload, including a Vector Field Magnetometer (VFM), an Absolute Scalar Magnetometer, and a Langmuir probe (LP). The LP measures electron density/temperature at a sampling rate of 2 Hz. The VFM, whose sampling rate is 50 Hz, can provide continuous high-resolution and precision magnetic field vector data. We mainly use 50 Hz VFM data of all three Swarm satellites in this study, and for some cases LP data are investigated as well. The data are available at the ESA web site (https://earth.esa.int/web/guest/swarm/data-access), which is open for worldwide users.

2.2. Data Processing

The Swarm Level 1b 50 Hz magnetic field vector data products are presented in the geographic North-East-Center (NEC) coordinate system. The small magnetic fluctuations at low and middle latitudes we are focusing on are practically limited to deflections perpendicular to the strong ambient field. For that reason, we transform the magnetic field data from the NEC frame into the Mean-Field Aligned (MFA) frame. In the MFA coordinate system, the z (parallel) component is along the mean magnetic field, y (zonal) is perpendicular to the mean magnetic field and horizontally pointing eastward, and x (meridional) completes the triad pointing outward (e.g., Park et al., 2008; Park, Lühr, Stolle, Rother, Min, & Michaelis, 2009). The mean background field is deduced by low-pass filtering the NEC frame data with a cutoff period of 60 s. From this smoothed ambient field we deduce the local declination and inclination, which are needed for the transformation from NEC to MFA frame. Actually, after transformation, the variations slower than 60 s are mainly removed from the MFA-y and MFA-x components.

In order to detect the small-scale disturbances in the ionosphere, we use a 1 s high-pass filter applied to the zonal magnetic field (y) component. The identified events are further analyzed in MFA coordinates, and the related field-aligned current (FAC) within an event is calculated. The method of FAC calculation follows the approach of Lühr et al. (1996) and Rother et al. (2007). The FAC density, j_z, is estimated

$$j_z = \frac{1}{\mu_0} \frac{\partial b_y}{\nu \, \partial t} \frac{1}{\sin I} \tag{1}$$

where μ_0 is the permeability of free space, ν is the spacecraft velocity, t is measurement time, and I is the inclination of the geomagnetic field. Any variation of the eastward, b_y component is interpreted as spatial field gradient caused by a long FAC sheet oriented in east-west direction. Temporal variations over some tens of seconds are assumed to be negligible. FAC densities with positive sign represent currents flowing along the magnetic field, that is, upward in the Southern Hemisphere and downward in the Northern Hemisphere. For reducing the effect of the 50 Hz digitization noise on the results, the FAC curves have been low-pass filtered with a 3 Hz cutoff. This frequency has been identified as the optimal trade-off between not modifying the FAC shape and reducing the noise.

3. Observation of Small-Scale Events

Before analyzing the typical characteristics of the small-scale magnetic fluctuations, we introduce here first the detection approach and then describe the detailed features based on typical events.

3.1. Event Detection Approach

As described above, we make use of the magnetic field vector data in MFA frame. The 50 Hz zonal (y) component data, high-pass filtered with 1 Hz cutoff, is taken for event detection. Due to the very low noise level (10–20 pT rms) of the VFM, any fluctuation above a threshold of $\pm$ 0.2 nT can be treated as a point of concern. If at least four successive points exceed the threshold in the filtered y component, a subevent is defined. Further detected points, exceeding the threshold, in the range of 15 s before and after the initial detection are integrated into the subevent. Therefore, the subevent's boundaries are extended to include the additional points. Then the procedure is repeated searching for active points within a range of $\pm$15 s outside the new boundaries. If no concerned points are found within that range, the group of data points is taken as an event. A computer algorithm was developed to identify the SSTID events in the high-pass filtered 50 Hz MFA y component.
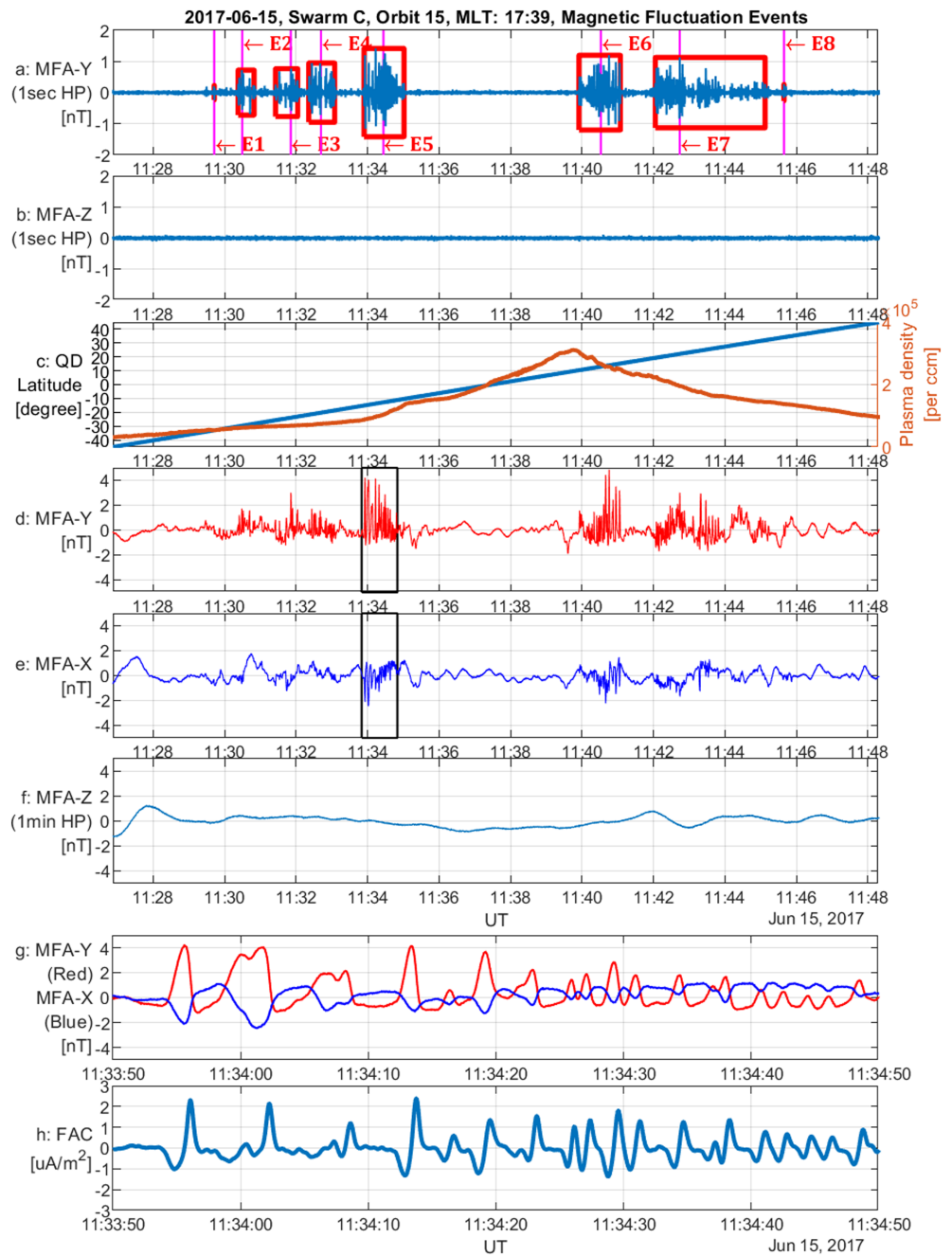
Figure 1. An example of SSTID events at dusk. (a, b) 1 Hz high-pass filtered *y* and *z* components of magnetic field in MFA coordinates. Red boxes in (a) mark the detected events; (c) plasma density measured by Swarm/EFI and quasi-dipole (QD) latitude of the satellite position; (d, e, f) *y*, *x* components and 1 min high-pass filtered *z* component in MFA frame; (g) zoomed details of the event marked by the black box in (d) and (e); (h) the estimated FACs.

3.2. Introduction of Individual Events

Figure 1 shows a typical example observed on 15 June 2017 by Swarm C in the evening sector on an upleg pass. In Figure 1a, each detected event is marked by a red box. Its width represents the duration of the event, and the height reflects the peak-to-peak amplitude. A magenta line indicates the weighted center of an event time considering the variation of its magnitude. The 2 Hz sampled plasma density data, measured by Swarm/EFI, are plotted in Figure 1c. It shows the equatorial ionization anomaly with a large crest in the Northern (summer) Hemisphere, but a very small peak in the Southern Hemisphere, around $\pm 10°$ QD latitudes. There are no

obvious fluctuations observed either in the plasma density or in the filtered MFA z component corresponding to the SSTID events. The blue line in Figure 1c indicates the magnetic latitude of the measurements. Here we use the QD latitudes of the Magnetic Apex system, as defined by Richmond (1995). It can be seen that in this case the events tend to appear symmetrically about the magnetic equator at conjugate latitudes. In the panels below (Figures 1d–1f) the unfiltered MFA components are shown. The small-scale fluctuations are most prominent in the eastward, y component (up to 4 nT), and the deflections are mainly in positive direction. Some correlated variations appear in the x component but nothing in the field-aligned z component. We take this as an indication that the magnetic fluctuations are caused by FAC filaments. The bottom panels (Figures 1g and 1h) provide a further blowup of the event marked by the black box. Here we see a series of separated small-scale deflections. The x and y components vary in antiphase, indicating a certain tilt of the FAC sheets. The bottom curve shows the estimated FAC density along the orbit. Quite prominent are the positive FAC peaks reaching amplitudes of about 3 μA m^{-2}. The full width at half-maximum of their horizontal scale amounts to about 4 km. These narrow FACs in the Southern Hemisphere are flowing upward, but they are accompanied by downward currents on the poleward sides. These return currents, extending over larger latitude ranges, have smaller amplitudes but carry a comparable amount of total current. The individually balanced current loops are the reason for the unipolar magnetic deflections of the x and y components.

Figure 2 shows an example from 27 June 2018 observed by Swarm C in the morning sector. Also on the dayside we find prominent SSTID events. In this case the plasma density around the equatorial ionization anomaly is well developed and shows a more typical symmetrical shape. But again, there is no obvious plasma variation related to the small-scale magnetic fluctuations. Clear plasma density undulations, for example, around 00:42 and 00:59 UT, occur outside of our event times. During the prenoon hours the magnetic deflections are commonly larger than on the nightside, and they again tend to appear at conjugate latitudes in the two hemispheres. In the field-aligned, z, component we observe smooth oscillations, which are probably driven by upstream waves, as described by Heilig et al. (2007). Another difference is that the small-scale saw-tooth structures of the y component are deflected westward. The steeper field gradients appear on the poleward side. Although the magnetic deflections are larger, the peak FAC densities are on average smaller than before sunset. They reflect intense upward currents in the Southern Hemisphere, which are accommodated by broader downward FACs on the equatorward side, carrying the return current. The latitudinal FAC sheet sequence is opposite to the one resulting from Figure 1.

Our detection algorithm finds also other events that are not related to SSTIDs. We have tried, by introducing extra tests, to exclude those as good as possible. One example of false detection is the crossing through an ionospheric plasma irregularity. Any event in which the parallel component MFA-z shows small-scale fluctuations typically accompanied by plasma fluctuations will be identified as an equatorial plasma bubble (EPB) (e.g., Stolle et al., 2006). Such events have been excluded. As an example, Figure 3 shows a low-latitude pass in the 21 MLT (magnetic local time) sector of Swarm A. We can see that the events EB1, EB2, EB5, EB6, and EB7 are confirmed as EPBs by our algorithm. However, E3 and E4, close to the equator, failed to be rejected due to the weak signal in MFA-z (<0.15 nT) and the low plasma density. In spite of these limitations, the large majority of EPB events are excluded.

Another type of false event is high-frequency magnetic pulsation. According to Park et al. (2013), Pc1 pulsations are geomagnetic fluctuations in the frequency range 0.2–5 Hz, which can be observed at midlatitudes. To avoid contamination by these pulsations, the detected SSTID events are checked by the methodology described in Park et al. (2013). The fast Fourier transform spectrum of an event is checked for frequency content in the Pc1 range with amplitudes larger than 0.05 nT. The spectral peak has to be localized in frequency, and the amplitudes below 0.2 Hz have to be smaller than the wave spectral peak. Typical Pc1 cases identified in this way are picked out. Figure 4 shows an example of this checking procedure. Swarm A crosses around 10:06 UT an event in the 06:30 MLT sector that exhibits an isolated peak in the fast Fourier transform spectrum. A further blow-up of the magnetic recordings reveals the typical signatures of a Pc1 wave packet; harmonic oscillations at about 0.6 Hz are mainly confined to the y component and no wave signal in the total field (z component).

Besides excluding plasma bubbles and Pc1 events, the quality flags of the 50 Hz Swarm VFM data were also considered. However, we could not find any correlation between the flags and our event detection. With all these efforts, we think, we have compiled a quite reliable list of SSTID events.
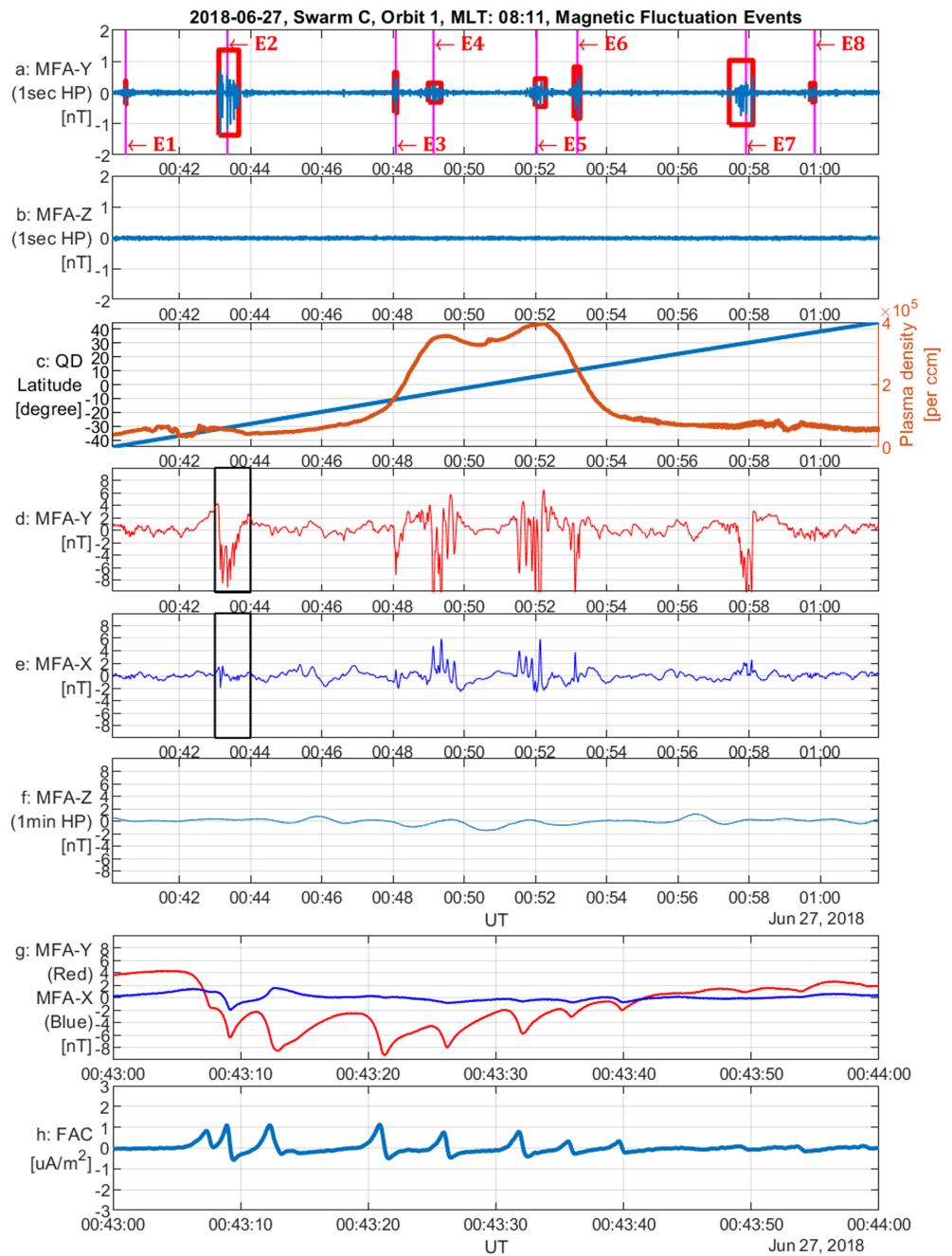
Figure 2. Same format as Figure 1, but for SSTID events in the prenoon sector.

4. Statistical Analysis of SSTID

After having described the typical characteristics of individual events we present in this section the mean properties of SSTIDs. The time period covered for this study lasts from January 2015 to December 2018, which is four complete calendar years except for a few days of missing data. To avoid misinterpretation of magnetic fluctuations, the data from 2013 and 2014 are not used due to several activities for orbit maneuvers and in-flight calibration activities during the initial mission year. From the start of 2015 to the end of 2018 the LTAN of the Swarm A and C orbits went 5.5 times through 00:00–24:00 local times. In the case of Swarm B, the LTAN covered only 5.2 times all local times (see Figure 6). On the descending node of each orbital arc the satellites pass again multiply through all local times. Both arcs together provide a good local time coverage during all seasons. We focus on event detection in the midlatitude and low-latitude regions
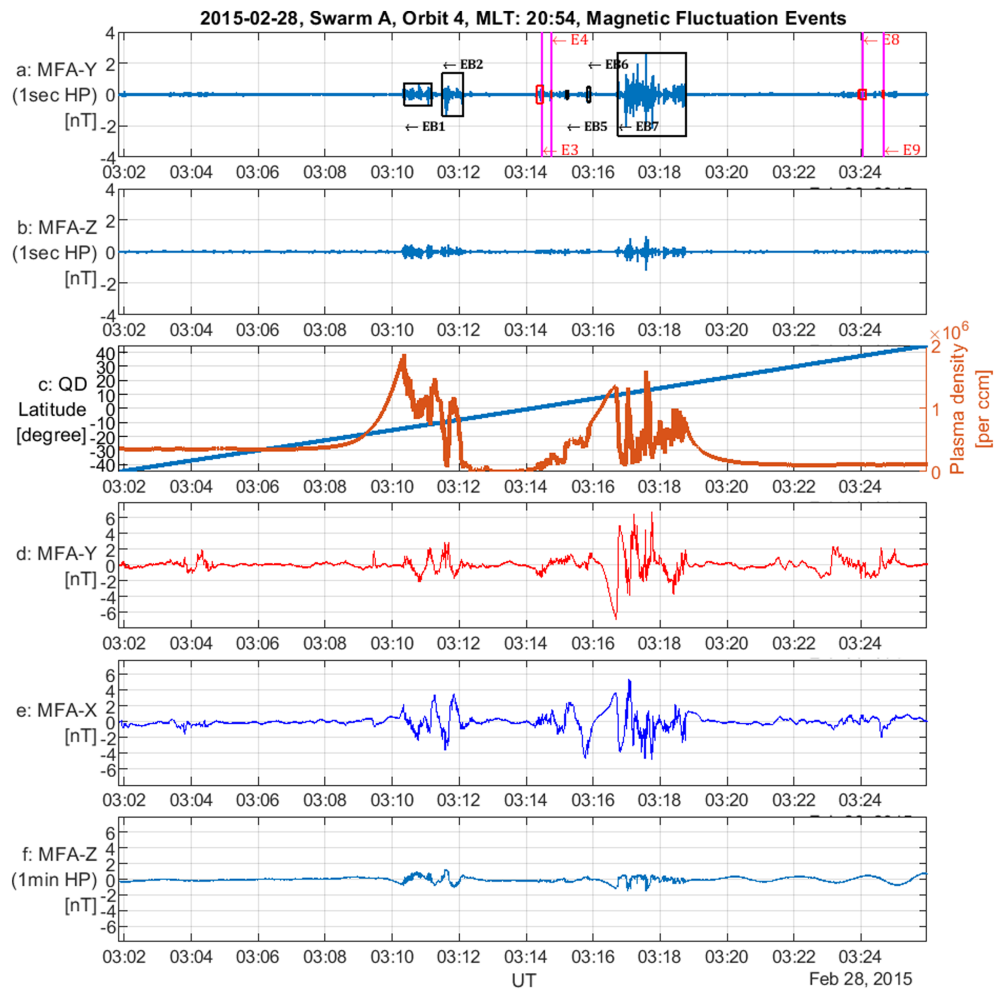
Figure 3. An example of a pass that includes plasma bubble events (black boxes). These are excluded from our event collection. For format details see Figure 1.

from −45° to 45° QD latitude because our small-scale magnetic fluctuation cannot easily be distinguished from FAC signatures in the auroral and subauroral regions.

4.1. Detections of SSTID Over Swarm Mission

All the detected events of the years 2015–2018 have been stored with their relevant information (time, geographic longitude and latitude, QD longitude and latitude, magnetic local time of the weighted center, duration, and intensity of the event and corresponding FAC intensity). During the study period Swarm circled the Earth about 22,000 times. That means more than 44,000 orbital arcs per satellite have been scanned. As shown in Figure 5b, about 35% of the orbits are affected by SSTIDs. On average there are a little more than two events per affected orbit arc. The event numbers are quite evenly distributed among the three spacecraft, just a little fewer at the higher Swarm B. There is no significant dependence of the SSTID occurrence rate on solar activity ($F_{10.7}$) observed, as can be deduced from Figure 5, just a few more detections during the latter two years. Conversely, the number of identified EPB events in Figure 5b is highly correlated with $F_{10.7}$, confirming the dependence of EPBs on solar activity.

We have also looked into the day-to-day variation of the event rates. Figure 6 shows the counts separately for the three spacecraft over all the years. There is an obvious variation of this rate observed from around 60 events per day to almost none. A certain relation of the count rates to the local time of the orbit (saw-tooth curves on top) can be deduced, but it is not very systematic. All this indicates that SSTIDs are dependent both on local time and season. For resolving the various dependences of SSTIDs larger statistics have to be considered.
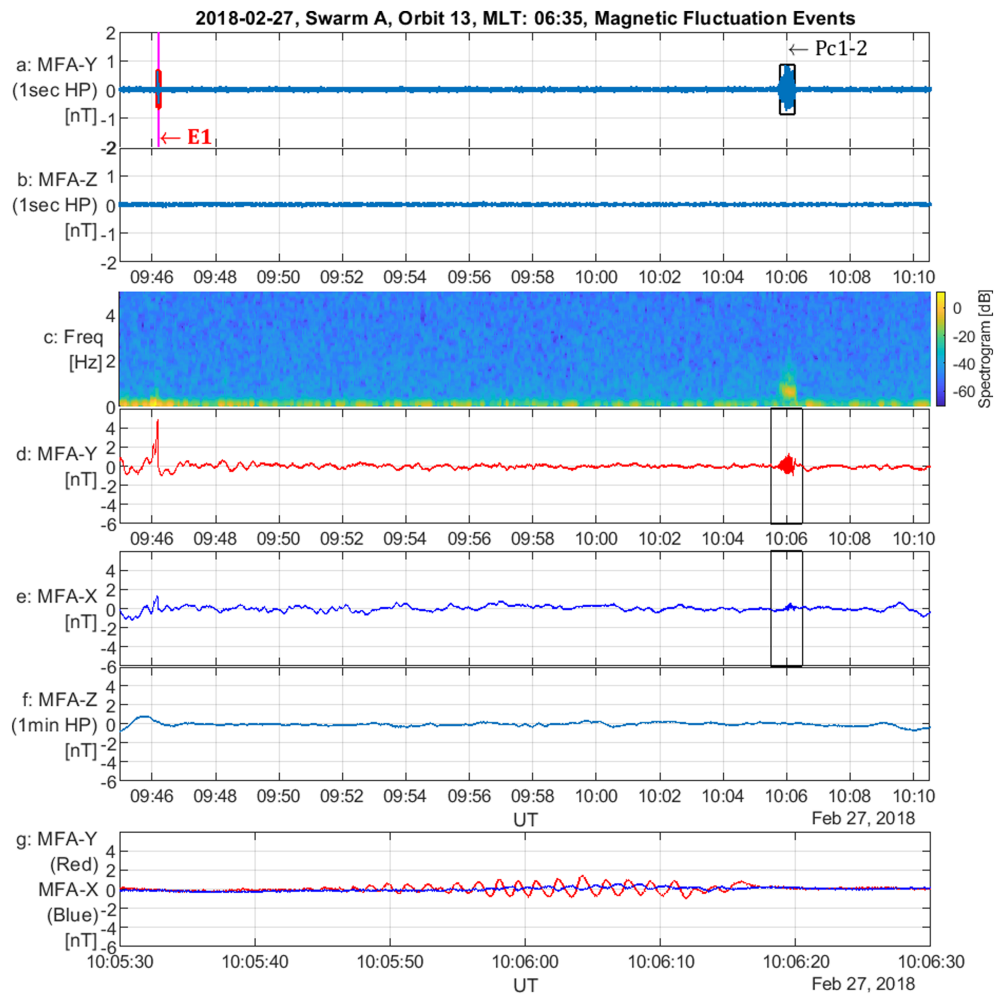
Figure 4. An example of a pass that includes a Pc1 pulsation event (black boxes in panels a, d, e). This is excluded from our event collection. The format is similar to that of Figure 1, but panel c shows the dynamic spectrum of the *y* (panel d) component.

4.2. Global Distribution of SSTID Events

In the previous subsection, we saw that the events are rather evenly distributed over the years. For that reason, it is justified to combine the events from the whole period in one day-of-year file. By that procedure a possible beating between local time and seasonal dependence will be mitigated and the statistical significance improved.

In a first step we look into the global distribution of the SSTIDs. Every detected event is sorted into bins of size 5° in geolongitude by 0.5° in QD latitude. The number of events in each bin is called event density. Subsequently, the event density map is smoothed by a 2-D median filter. That means the number of events in a bin is replaced by the median value of 54 neighboring bins, forming a rectangle of nine latitude by six longitude bins around the center grid. This helps to remove longitudinal stripes that result partly from repeat orbits.

7Figure 7 shows the derived global distribution of events separately for the three spacecraft. All three frames provide rather similar results. The highest event densities are observed over East Asia and Australia around northern and southern 30° QD latitude. These occurrence maxima can be regarded as magnetically conjugate. A secondary occurrence peak appears over the North Atlantic Ocean, for which no counterpart can be found in the south. Rather, there is a distinct trough in event density from −90° to 60° longitude (from northern Chile to the Cape of Good Hope) in the Southern Hemisphere. This bite-out in event occurrence coincides well with the SAA of the geomagnetic field. A void of events appears also at
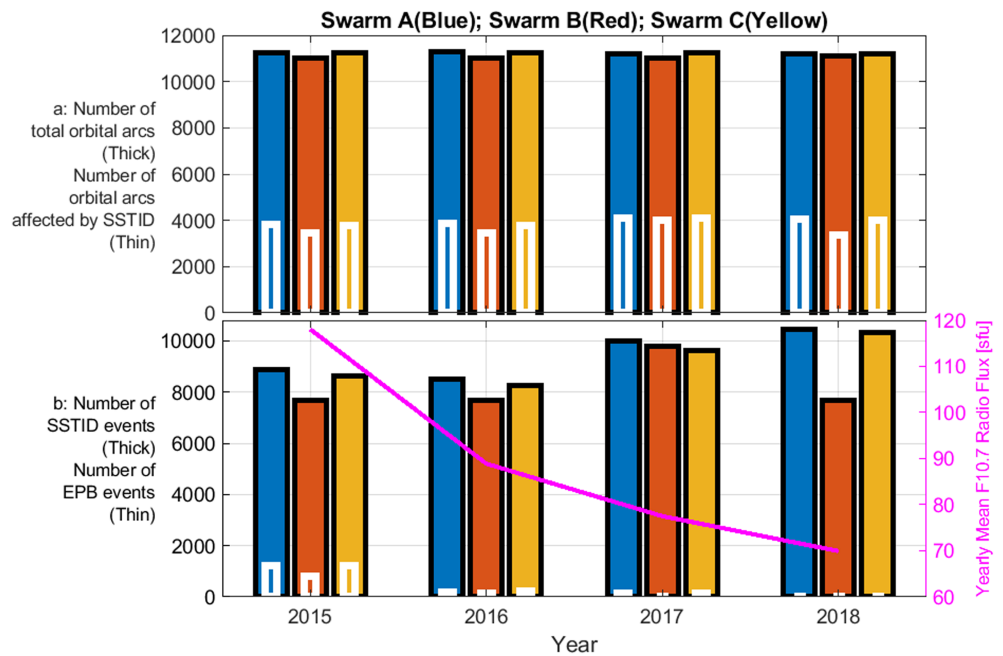
Figure 5. Statistical properties of our event collection, separately for each year and the three Swarm satellites: (a) total number of orbital arcs and number of orbital arcs affected by SSTID; (b) total number of detected events and number of detected EPB events, in comparison with the mean solar activity evolution.

low magnetic latitudes within about ±10° QD latitude, with the exception of an occurrence patch near the northeast coast of Brazil. This is attributed to an imperfect exclusion of EPB events, and they should be ignored in further considerations. Support for this interpretation come from the much-reduced equatorial event density in this area from the higher-flying Swarm B recordings. Other examples of unrelated events are the occurrence peaks in the North Atlantic at highest latitudes and south of Australia at southern
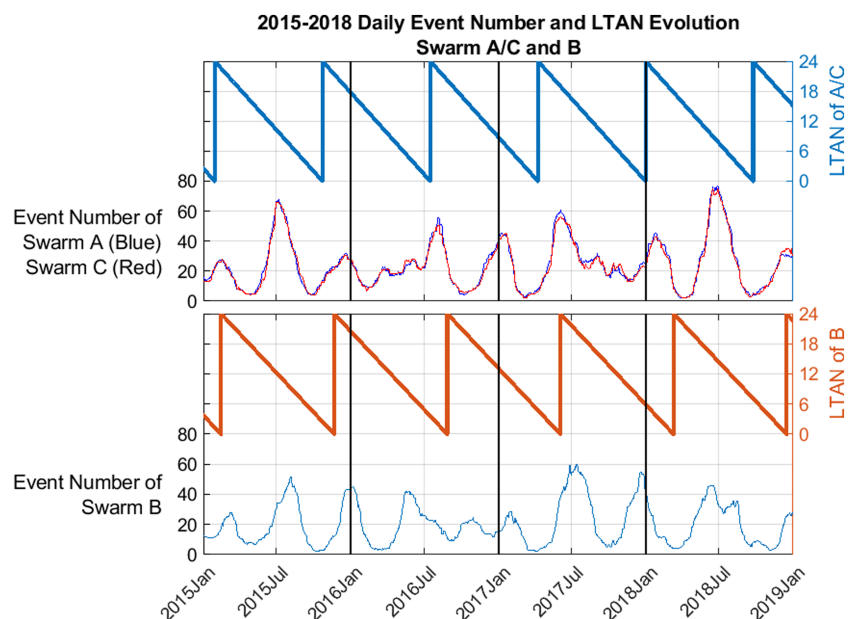

Figure 6. Temporal variation of event numbers (30 days moving median) separately for the three Swarm satellites in comparison with the local time (LTAN) evolution of Swarm A/C (top) and Swarm B orbits (bottom).
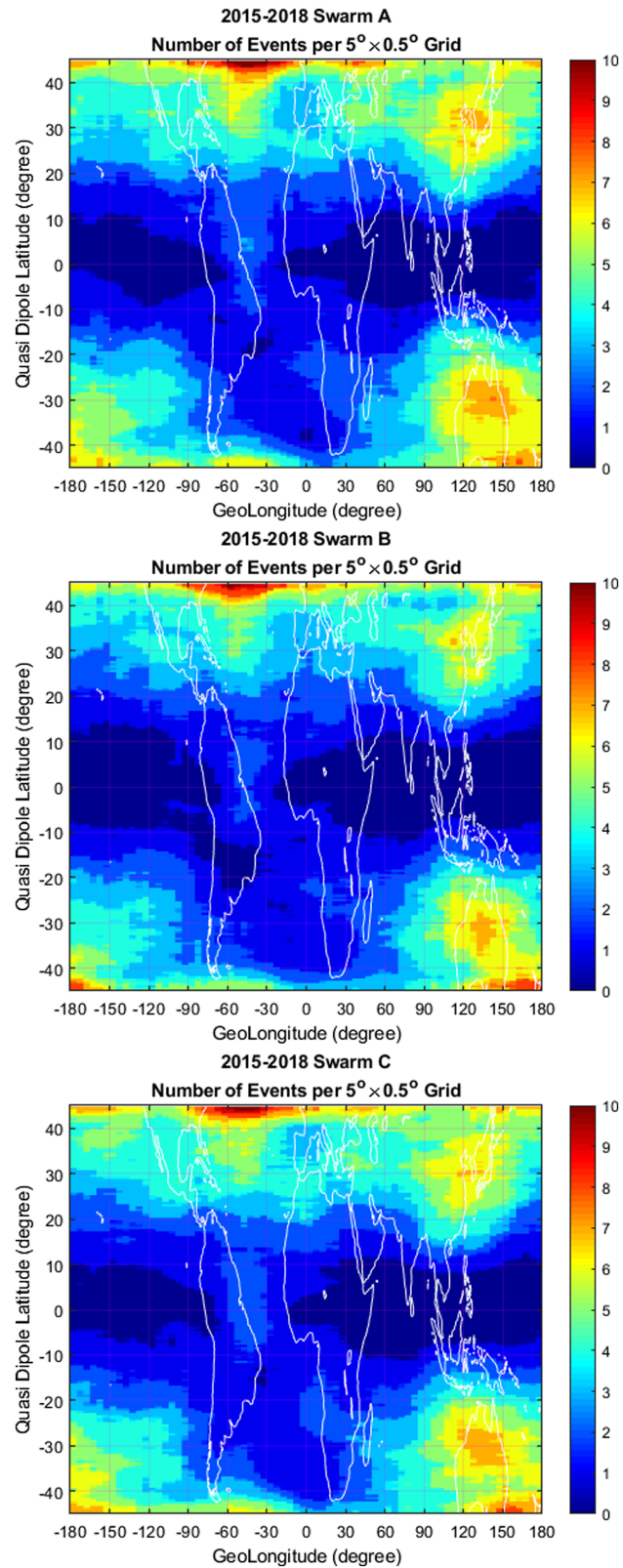
Figure 7. Global distribution of SSTID event number density in geolongitude versus QD latitude frame (gridded 5° longitude by 0.5° QD, smoothed over 30° longitude by 4.5° QD moving median) separately for Swarm A, B, and C. Continental contours are added in the frames.
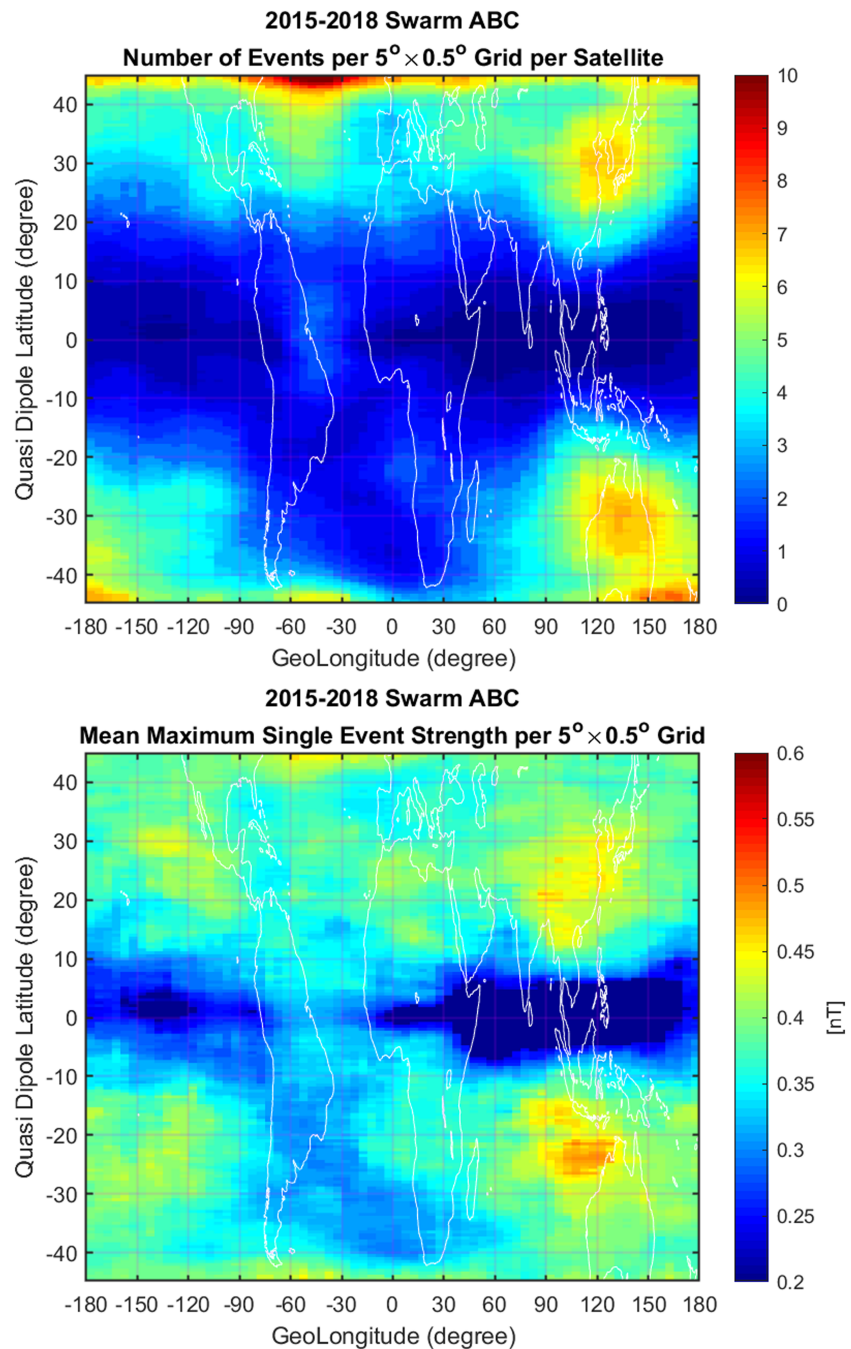
Figure 8. (top) Same format as Figure 7, but for combined event number density from Swarm A, B, and C. (bottom) Global distribution of mean maximum event amplitude in longitude versus QD latitude frames (same resolution and smoothing as in Figure 7).

latitudes. These appear on longitudes close to the magnetic poles and are probably due to effects of sub-auroral current systems.

By comparing the global distributions of the SSTIDs from the three Swarm satellites in Figure 7, we find a high degree of similarities. This is taken as motivation for combining the event detections from all three satellites for achieving an average picture of the SSTID distribution. By that we further improve the resolution and statistical significance. Figure 8 (top) shows the obtained average global distribution of event numbers, which well reflects the individual observations of the three spacecraft. All the following distribution maps are based on the multispacecraft averaged results.

For comparison, Figure 8 (bottom) presents the global distribution of the mean small-scale event peak amplitudes (deduced from the heights of green boxes, e.g., in Figures 1 and 2). Also in this case, the same 2-D median smoothing filter has been applied. The resulting picture is somewhat different from that of the event density, but there are also some similarities. Generally, larges amplitudes are found in the latitude range between 20° and 30° QD latitude, and the amplitudes are on average somewhat larger in the Southern Hemisphere than in the Northern Hemisphere. The geographic distribution of intensity is quite similar to that of the occurrence rate (top frame). The largest average amplitudes are found over East Asia and Australia. Secondary peaks appear over North America and the southern Central Pacific. The few events detected in the SAA region have small amplitudes. Also, the falsely detected EPBs near the magnetic equator have weak signals.

4.3. Local Time Dependence of SSTIDs

After we have seen the global distribution, we look now at the local time dependence of SSTIDs. As shown in Figure 9 (top), the event density peaks after sunset, between 18 and 22 MLT, in both hemispheres. Toward higher latitudes the occurrence peak appears at later time. A secondary weaker peak in occurrence rate shows up between 8 and 12 MLT in both hemispheres. Overall, the peaks in the Northern Hemisphere are stronger than those in the Southern Hemisphere. This is primarily due to the absence of SSTIDs in the region of the SAA. An imperfect exclusion of EPB events results in the double-peak structure near the magnetic equator around 22 MLT. When ignoring those, the void of events at low latitudes stands out clearly. The false detections at subauroral regions (top and bottom fringes) are concentrated around noontime. From this figure it is apparent that SSTIDs exhibit a distinct occurrence distribution focused mainly around the time from sunset to midnight, and on the dayside, they are concentrated around prenoon.

Also here, Figure 9 (bottom) presents the local time distribution of the mean peak amplitudes of our SSTID events. We find a clear dominance of more intense events at daylight hours compared to nighttime. There is a trough in amplitude around the 14 MLT sector, which seems to separate the events with evening to night characteristics from those in the morning to prenoon sector. The SSTID events in daylight have clearly larger magnetic amplitudes than those in darkness, regardless whether they belong to the prenoon or evening-night class. This is probably caused by the higher ionospheric conductivity in sunlight, even though many more events are detected after sunset.

4.4. Seasonal Dependence of SSTID

Figure 10 (top) presents the distribution of event density over the course of a year. SSTIDs clearly prefer the solstice seasons. Really outstanding is the high occurrence rate around June solstice in the Northern Hemisphere. Obviously, more events are found in the summer than in the winter hemisphere. During the months around December the weaker and almost equal event density in the two hemispheres is obviously caused by the lack of events in the south around the SAA. Very few events appear at the equinoxes. Also here, we find a rather distinct seasonal pattern of SSTID events.

When looking into the day-of-year variation of SSTID amplitude (see Figure 10, bottom) we find again the preference of solstice seasons. But interestingly, there are larger amplitudes during June solstice in the Southern Hemisphere than in the northern summer hemisphere. Therefore, the above argument about the role of ionospheric conductivity on event amplitude may not explain the full story. There must be additional processes at work that cause the larger magnetic deflections in the Southern Hemisphere. This dominance of southern amplitudes can also be observed during the months around December. It should be noted that only the small-scale structures (<10 km) have contributed to the mean amplitude distribution in these plots.

4.5. Distribution of Intense Small-Scale FACs

All the transverse magnetic signatures that we study here are interpreted as caused by FACs. At Swarm altitudes the perpendicular conductivities are by many orders of magnitude smaller than the field-aligned. For quantifying the current intensity, we have taken the peak value of FAC estimates from every event. No FACs have been calculated between $\pm 8°$ QD latitude. At these low latitudes the angle between orbit track and field lines is too small for a reliable current estimation. These zero-event bins are shown in deep blue in Figure 11. As we know from the SSTID examples in Figures 1 and 2, the narrow-scale FACs come with larger amplitudes compared to the broader return currents. The resulting distribution of events will therefore reflect the mean amplitudes of the large FAC peaks.
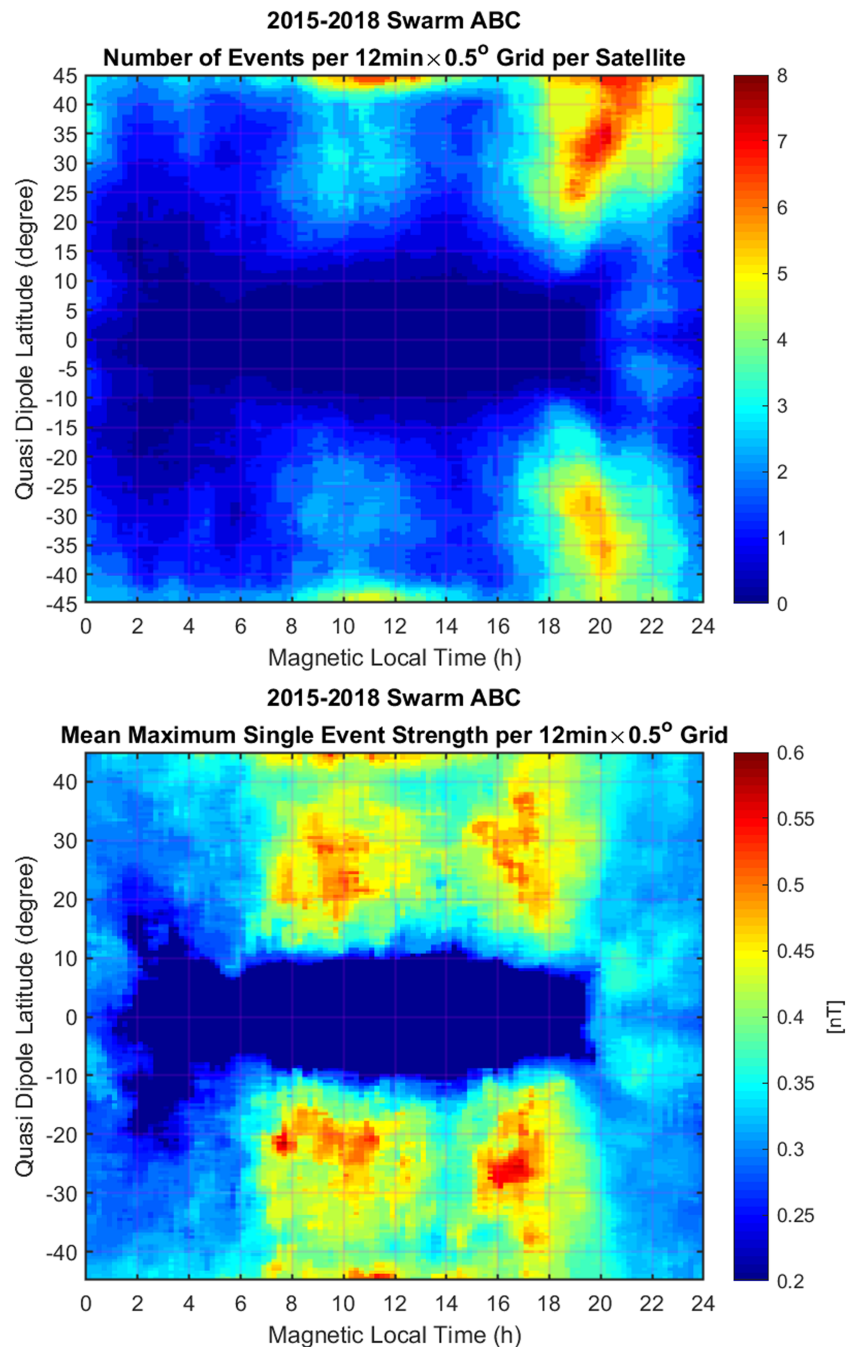
Figure 9. Same format as Figure 8, but for latitude distribution versus magnetic local time (gridded: 12 min × 0.5° QD, smoothed: 1 hr × 4.5° QD moving median).

In Figure 11 we show side by side the latitudinal distribution of the FAC peak amplitudes (left column) and event occurrence rate (right column) separately for the events with positive and negative FAC peaks. As before, these distributions are plotted from top to bottom versus geolongitude, magnetic local time, and day of year.

In general, we find a strong increase of large current amplitudes toward low latitudes. This suggests that the TID structures steepen as they propagate equatorward and by that higher FAC densities are required for maintaining current continuity.
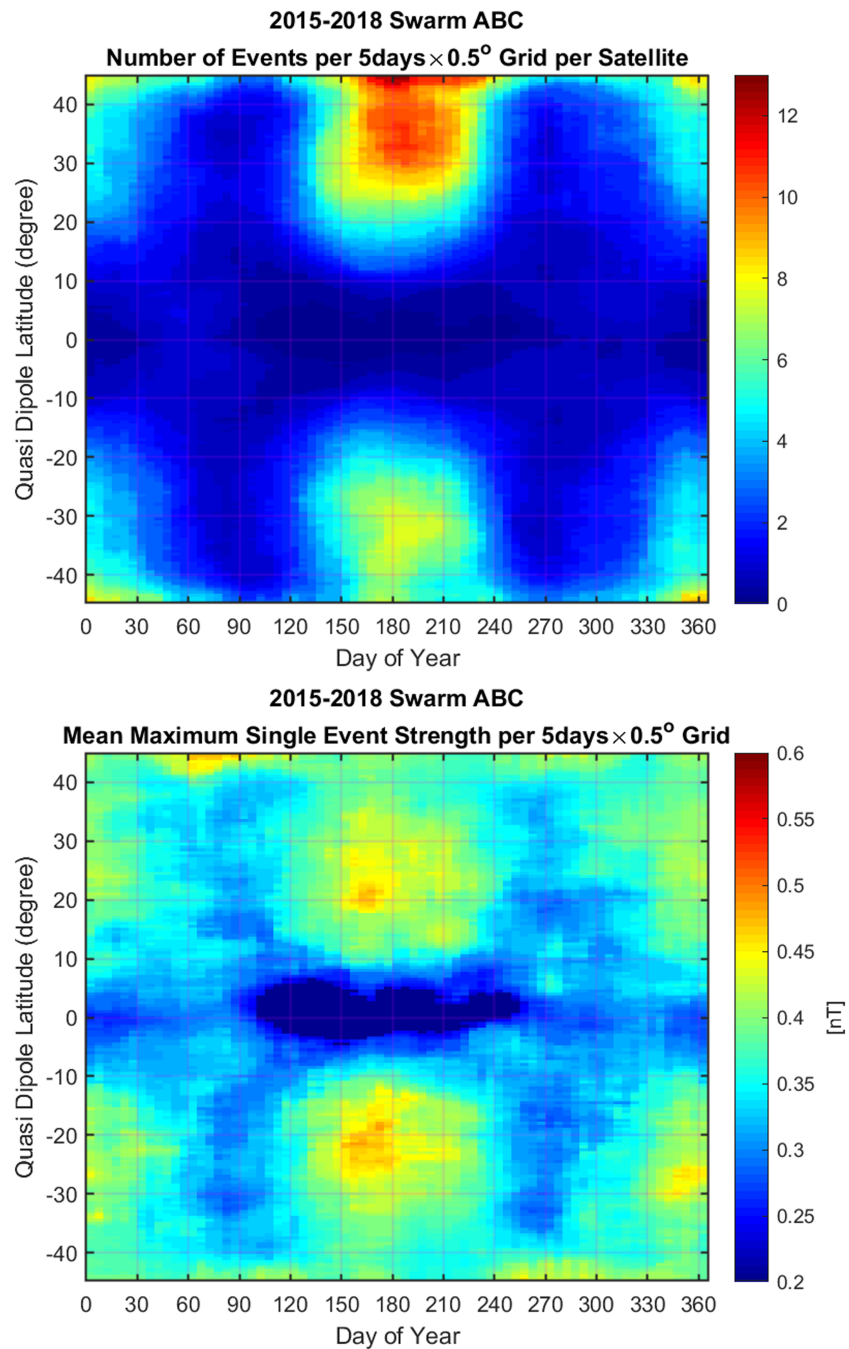
Figure 10. (top) Same format as Figure 8, but for latitude distribution versus day of year (gridded: 5 days × 0.5° QD, smoothed: 30 days × 4.5° QD moving median).

Figures 11a1 to 11a4 show the global distribution of FAC peak amplitudes. The largest amplitudes are recorded in the East Asian sector (100–150°E), for both positive and negative peaks. A secondary maximum appears in the western Pacific (120–150°W), more prominent for positive FAC peaks. In the longitude sector of the SAA (0–90°W) there is a clear hemispheric unbalance between the current amplitudes. Only weak FACs are observed in the south. The occurrence distributions of FACs is shown in the right column (Figures 11a2 and 11a4), reflecting well the event distribution of Figure 8. The plots for the distributions of positive and negative FAC peaks are very similar. We just find a few more cases with negative FAC peaks.
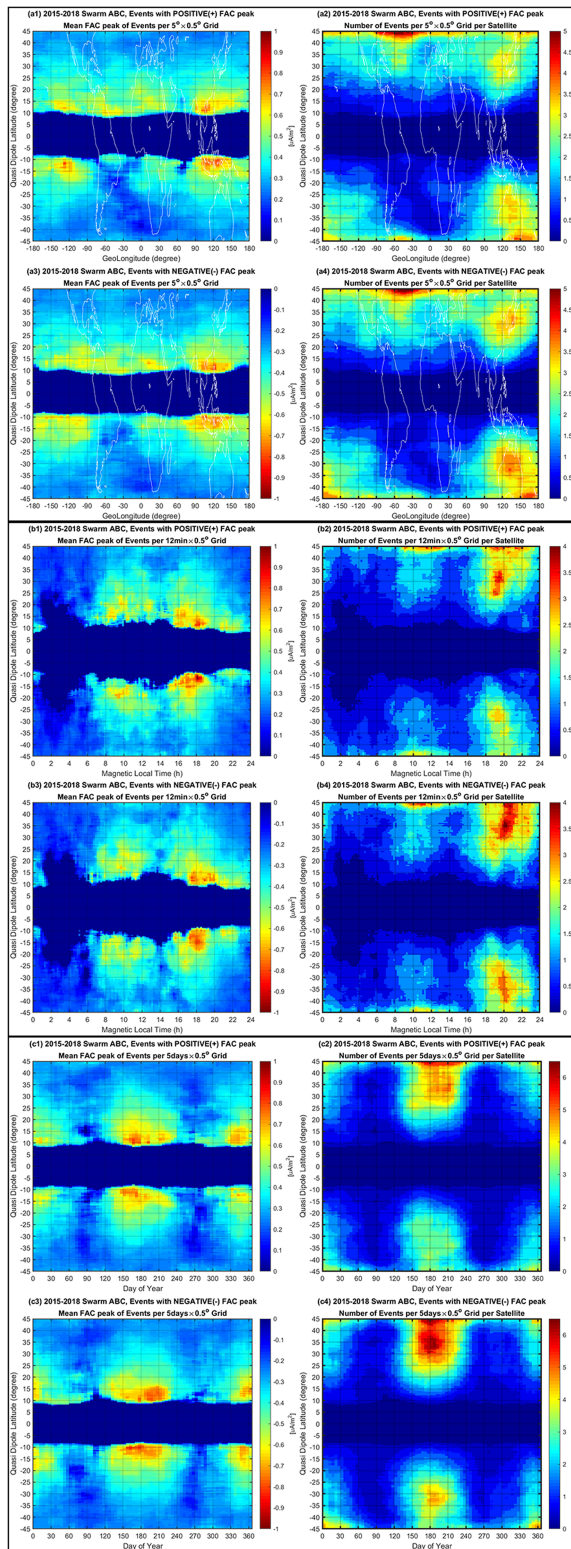
Figure 11. (a1, a3, b1, b3, c1, c3) Latitude distribution of the mean FAC peak amplitudes versus longitude, MLT, and day of year, separately for events with positive and negative FAC peaks. (a2, a4, b2, b4, c2, c4) Latitude distribution of number densities for events with positive and negative FAC peaks, also versus longitude, MLT, and day of year (same resolution and smoothing as in Figures 8–10).

When looking at the local time distribution of FAC intensity (Figures 11b1 and 11b3) a clear difference between the morning-prenoon and evening-night events can be found. On the nightside the focusing of large FAC peaks at low latitudes is much more pronounced. The dayside events exhibit more moderate FAC amplitudes, which are spread wider in latitude. This is in some sense in contrast to the large magnetic deflections in the sunlit sector. Obviously, the dayside magnetic signals exhibit smoother variations and are thus related to less narrow FAC structures with smaller current peaks, even though the total current flowing in the individual loops is, according to the greater magnetic amplitudes, larger on the dayside than on the nightside. Also in these figures, the 14 MLT amplitude trough marks a boundary in FAC characteristics. During postmidnight hours (2–4 MLT) hardly any FACs are observed. This can be regarded as the second demarcation line between the morning/noon and evening/night SSTID events. In Figures 11b2 and 11b4 the number density distribution of positive and negative FAC peaks is shown. Again, we find very similar patterns for the two polarities of FACs and the typical local time distribution of SSTID events. The large majority (almost 90%) of the events is found after 18 MLT, but those exhibit only small amplitudes.

The FAC peak amplitudes do not show a large difference between June and December solstices (see Figures 11c1 and 11c3). During equinoxes the amplitudes are largely reduced. This is probably attributed to the few events occurring in those seasons (see Figures 11c2 and 11c4). Also here, we find very similar distribution for positive and negative FAC peaks, just more negative FAC events.

In equation (1) we normalize the FAC densities, estimated at the various latitudes, by dividing the values by the sine of the inclination angle (Lühr et al., 1996). This factor is needed to account for the changing angle between Swarm orbit and geomagnetic field lines. When approaching low latitudes this factor will also increase the FAC noise. However, we argue that our 3 Hz filter will reduce the noise, and the focusing on the FAC peak amplitudes secures that the shown increase of FAC amplitudes toward low latitudes is a real effect.

5. Discussion

In the previous section we have presented the average properties of SSTIDs. From the individual events it is apparent that magnetic deflections have a sawtooth shape. In the evening example, shown in Figure 1, the steep ramps appear mostly on the equatorward sides in both hemispheres. The steep ramp is typically associated with a narrow FAC sheet of a few kilometers width and peak current densities up to 3 $\mu A\ m^{-2}$, which is a very large value for low latitudes. Conversely, in the morning example, shown in Figure 2, the narrow FAC sheets appear on the poleward sides. In this case the FAC peak amplitudes are not so large as in the evening event. Figure 12 provides a schematic drawing of the different FAC configurations for the two examples.

It would have been tempting to suggest these different current configurations as typical for the two classes of events (morning-noon versus evening-night). However, from Figures 11b1 and 11b3 we know that positive and negative FAC peaks show on average very similar local time
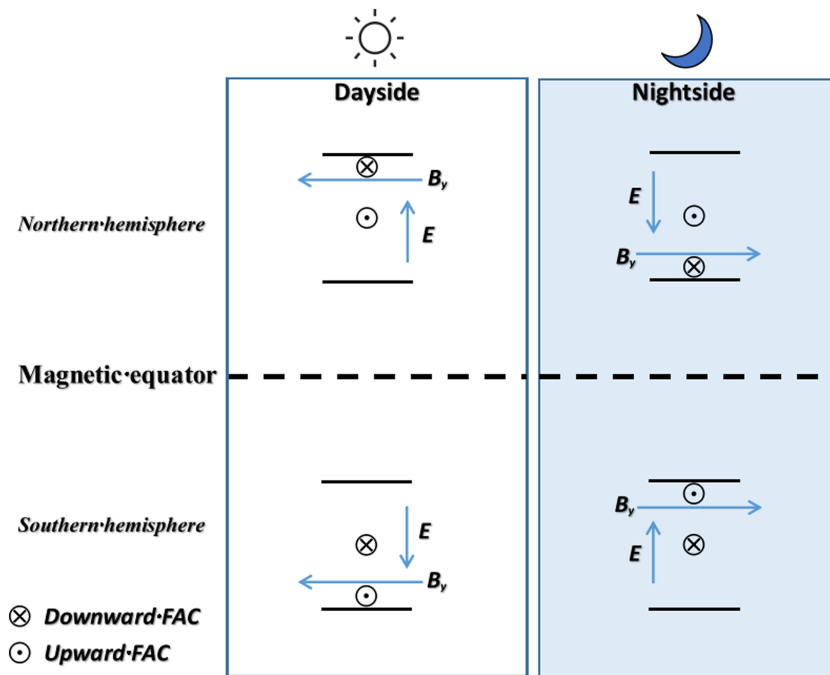
Figure 12. Schematic drawing of the FAC sheet distributions associated with the SSTID examples shown in Figures 1 (nighttime) and 2 (daytime).

distributions. Therefore, the two current configurations illustrated in Figure 12 can be found in both SSTID classes.

In a recent paper Park et al. (2016) deduced from the combination of Swarm electric and magnetic field measurements that around June solstice most of the nightside medium-scale TIDs exhibit a southward directed Poynting flux. That means, the generator region is in the north and the load in the Southern Hemisphere. Assuming that the same is true for the SSTIDs, we have added the resulting electric field vectors in Figure 12. On the dayside E fields point poleward, and in the evening/nightside sector they point equatorward. For our two examples the narrow and intense FACs flow in both time sectors into the Northern Hemisphere, which is according to Park et al. (2016) commonly the source region around June solstice. The transition time between the two E field directions in Figure 12 and the two SSTID classes, around 14 MLT coincides well with the change in thermospheric zonal wind from westward around prenoon to eastward at night (e.g., Lühr et al., 2012, Figure 4). Also, the directions of the suggested E fields are consistent with those caused by the zonal wind together with the vertical B field components in the two midlatitude hemispheres. Based on our statistical results, however, the ratio between narrow FACs flowing into (+FAC) and out of the Northern Hemisphere (FAC) is in the two local time sectors about the same (see Figure 11).

5.1. Spatial Scale of SSTID

We can make use of the simultaneous readings from the Swarm A and C satellite pair for deriving information about the azimuthal scale size and orientation of the SSTID structures. Figure 13 shows for three cases concurrent observations of y component variations. The observed events in the top frame, from evening hours, are dominated by medium-scale features. Swarm A (orbiting 1.4° to the west of Swarm C) observed these negative deflections in both hemispheres slightly closer to the equator than Swarm C. This suggests a small tilt of the current structure away from east/west. The steep field gradients appear, in accordance with Figure 12, in all cases on the equatorward side. In the case of Figure 13, bottom frame, a dayside pass, medium-scale features are detected by Swarm A at higher latitudes in both hemispheres than by Swarm C. This implies a tilt of the current feature from northwest to southeast in the Northern Hemisphere and a tilt from southwest to northeast in the Southern Hemisphere, just rotated in opposite direction to the evening case. In this dayside pass all the steep magnetic gradients appear on the poleward sides.
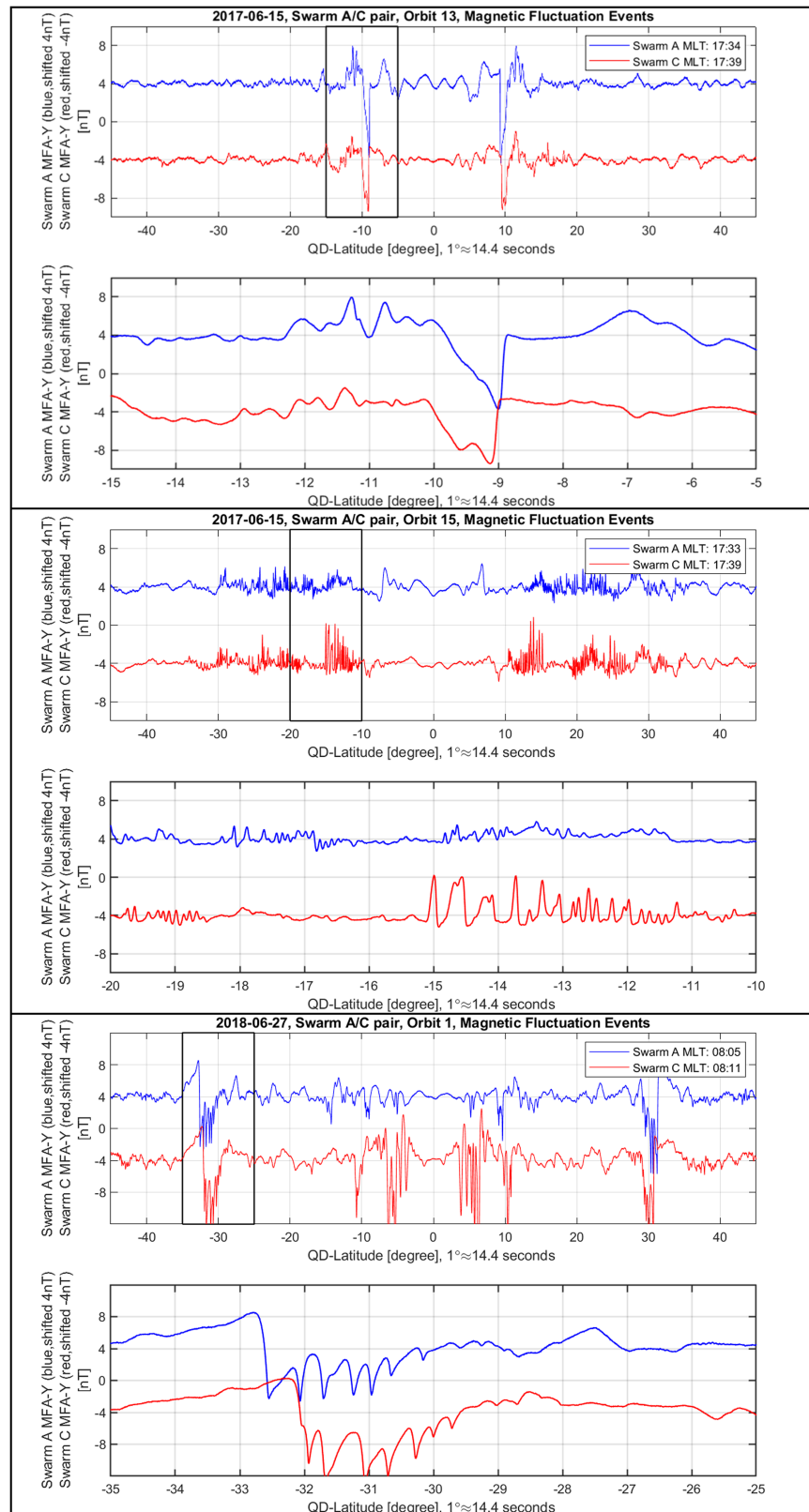
Figure 13. Simultaneously observed SSTID events by the Swarm A/C pair. Details of the magnetic variations in the black boxes are shown below. Swarm A flies at a distance of 1.4° in longitude to the west of Swarm C.

Opposed to the medium-scale structure the small-scale features show no obvious correlation between the observed events at the two spacecraft (see also Figure 13, middle part). Since the spacecraft are separated by about 150 km in east/west direction, the zonal extent of the SSTIDs must be shorter than that distance. The small features seem to be imbedded in medium-scale structures, frequently detected by both spacecraft but evolving locally.

From the relation between x and y component deflections one can deduce the local tilt of the SSTID current sheets. Commonly we find an antiphase variation of the two horizontal components in most of the events. This implies that the small-scale FAC sheets, different from the medium-scale structures, are preferably tilted from northwest to southeast (northeast to southwest) in the Northern (Southern) Hemisphere and at all local times; in combination of both hemispheres the structures should look like an inverted-C shape.

A special characteristic of these SSTIDs is the development of narrow and intense FAC sheets. There seems to be a typical minimum width of the sheet (around 5 km), at which the highest current densities are recorded. At auroral latitudes Rother et al. (2007) deduced a limiting scale size of about 1 km where the largest FAC densities are observed. Later Lotko and Zhang (2018) related these narrow high-latitude FACs with kinetic Alfvén waves. In their model they confirmed that the Alfvén wave power is attenuated at scales less than 1 km due to the finite parallel (collisional) conductivity. Our FACs at midlatitudes are probably not of auroral Alfvénic type, but still some kind of attenuation will be encountered at small scales as well, caused by other electrodynamic processes. For example, Forget et al. (1991) studied the scale dependence of the ionospheric closure current. They report that the effective height-integrated Pedersen conductivity is constant and equal to the classical Pedersen conductance for scales larger than 5 km. At smaller scales it shows a steep decrease of effective conductivity, limiting the closure current density. This effect can also be responsible for the finite dimensions of SSTIDs. Furthermore, Forget et al. (1991) studied the scale dependence of the ratio between magnetic and electric field fluctuations. When the scale sizes go down below 5 km, the ratio deviates from the expectations of classical Pedersen conductance. The smaller scale sizes, the fluctuations become more and more electrostatic, and the signatures can no longer be easily seen in magnetic field data. For example, assuming an MEF event whose scale size is larger than 10 km (medium-scale), the corresponding MMF activity is expected to be positively correlated with Pedersen conductance; that is, daytime medium-scale MMFs should be larger than nighttime ones. According to Forget et al. (1991), however, small-scale (<5 km) MMFs, as in our study, deviate from the expectations of classical Pedersen conductance. This may contribute to the fact that the ratio between small-scale FAC density and magnetic deflection is smaller during daytime than during nighttime. More dedicated studies are probably needed for fully exploiting the processes limiting the scale sizes.

5.2. Relation of SSTID to Medium-Scale Magnetic Fluctuation

In our analysis we identified two classes of SSTID events, the ones occurring around morning/noon hours and those in the evening/night sector. The average characteristics of the evening/night events have a lot in common with nighttime medium-scale TIDs. This can be summarized as follows:

1. As local time increases from dusk toward midnight, the event occurrence peak moves poleward. It seems to follow the day/night terminator line in the summer hemisphere. The same behavior can be observed for MSTIDs; compare our Figure 9 (top), for example, with Park, Lühr, Stolle, Rother, Min, Chung, et al. (2009, Figure 2d), and for sporadic E, see Page 10 of Arras and Wickert (2017).
2. The global distribution in Figure 8 (top) reveals highest occurrence rates over East Asia and Australia. A secondary maximum appears in the North Atlantic. Conversely, there is a void of SSTID events in the region governed by the SAA. All these occurrence features are consistent with those of medium-scale magnetic fluctuation (see, e.g., Park et al., 2015, Figure 3). Similarly, sporadic E layers show a bite-out in occurrence near the magnetic equator and at the SAA (e.g., Arras & Wickert, 2018). Sporadic E layers are commonly regarded as sources for MSTIDs (e.g., Swartz et al., 2009).
3. Also, for the seasonal variation of the occurrence rate we find compelling similarities. Both small- and medium-scale magnetic fluctuations are rare during equinoxes. They occur most frequently around June solstice and at somewhat lower rate during December months (compare our Figure 10 with Park et al., 2015, Figure 3; Arras & Wickert, 2017, p. 10; Kil & Paxton, 2017, Figure 3).

This high degree in communality infers a connection between these phenomena: small-scale MMF, medium-scale MMF, MSTID in topside plasma density, and sporadic E. We suggest that the small scales presented here are an evolutionary state of the medium-scale TIDs. As for the nighttime events, the steepening may be due to secondary instabilities caused by E field or wind effects on midlatitude plasma density gradients of MSTIDs (e.g., Kelley et al., 2004). As MSTIDs generally drift equatorward (Tsugawa et al., 2007, Table 1), small-scale secondary structures (and related narrow FAC structures) are expected to become more confined and stronger toward low latitudes (i.e., at a later stage of the evolution). This process seems to terminate when horizontal scales of about 5 km and highest FAC densities are reached. From Figure 11 we know that FAC peak amplitudes, in particular for nighttime events, get larger toward lower latitudes, that is, structures get narrower. However, there appears a limiting latitude around $\pm10°$ QD latitude, where practically no more SSTIDs are observed by Swarm. When mapping this location down along field lines to the E region (110 km) we obtain a lowest latitude for the generator region at about 16° QD latitude. Note that MSTIDs, the alleged source of SSTIDs, have general difficulty to reach equatorward of about 18° MLAT, see Discussions of Sivakandan et al. (2019) and references therein. Furthermore, ionospheric dissipation processes are probably responsible for the termination of irregularities at this boundary. We claim that the present picture of nighttime MSTIDs has to be extended toward smaller scales down to a few kilometers.

In the case of our morning/noontime events it is difficult to find dedicated studies focusing on dayside MSTIDs. Frequent arguments are that it is difficult to distinguish the MSTID fluctuations from other electric and magnetic activities during sunlit hours (e.g., Heilig et al., 2007). Our approach of limiting the detections to small-scale magnetic structures may mitigate the ambiguity. In the following we compare our results with studies investigating the characteristics of daytime medium-scale magnetic fluctuations without any data selection.

Let us take, as examples, the climatology of medium-scale MMFs presented by Nakanishi et al. (2014) and Aoyama et al. (2017). Both studies are based on 1 Hz magnetic field data, which means they consider only variations with wavelengths larger than 15 km. A direct comparison may suffer from the different methods of data processing. In our study the "amplitude," shown in Figures 8–10 (bottom), is defined as the mean of the small-scale maximum amplitude of selected events. On the contrary, the "amplitude" of Nakanishi et al. (2014) and Aoyama et al. (2017) was obtained without event selection; the mean is calculated from all satellite passes. No attempt was made to focus on a dedicated generation process. The term "amplitude" in Nakanishi et al. (2014) and Aoyama et al. (2017) represents rather a combination of our number of events (top panels of Figures 8–10) with the mean maximum amplitude of events (bottom panels). Nevertheless, we can deduce the following conclusions by qualitatively comparing our results with Figure 10 of Nakanishi et al. (2014) and Figure 2 of Aoyama et al. (2017). The most notable differences between the statistical results of our small-scale features and their medium-scale magnetic fluctuations are:

1. In Nakanishi et al. (2014) and Aoyama et al. (2017) dayside magnetic activity is clearly stronger than that of the nightside. On the contrary, we find a number of events clearly larger after sunset than during daytime, and the mean FACs amplitudes of the qualified events are comparable between the two local time sectors.
2. Nakanishi et al. (2014) and Aoyama et al. (2017) reported stronger activity in the American/South Atlantic sector than over East Asia/Oceania. On the contrary, our study exhibits the hottest spot of event occurrence over East Asia and Australia.
3. Nakanishi et al. (2014) and Aoyama et al. (2017) find large-amplitude activity in the region of the SAA, where we record a bite-out of events.

In short, the medium-scale MMFs analyzed by Nakanishi et al. (2014) and Aoyama et al. (2017) favor regions of high conjugated ionospheric conductivity, for example, the American sector. This longitude sector hosts in the south the global minimum of geomagnetic field strength, the SAA. The weak geomagnetic field can enhance Pedersen conductivity. As an example, E region conductivity at 22 LT reaches there its global maximum; see Figure 5 of Rodríguez-Zuluaga and Stolle (2019). As prime candidate for exciting the magnetic fluctuations the authors of these two works suggest upward propagating acoustic and gravity waves driven by meteorological phenomena. Although they did not perform any event selection, the characteristics of real daytime MSTIDs seem to be fully overridden by the other magnetic fluctuations.

The small-scale MMFs in our study exhibit a hot spot in occurrence rate over East Asia/Oceania and a bite-out in the SAA region. These characteristics may be explained by the suggestions of Ivarsen et al. (2019). Although that study focused on polar cap patches, their arguments may be applicable also for our work. According to Ivarsen et al. (2019) the dissipation of small-scale F region irregularities, connected to the conducting E region, occurs at the scale size of about (and smaller than) 5.8 km. This is close to the typical full width at half maximum of 4 km that we typically find for the small structures (see section 3.2). According to these authors small-scale MMFs are expected to be more persistent (or survive longer) under the conditions where E region conductance is lower. Medium-scale MMFs can exist on the dayside, but the concomitant development of small MMF scales is expected to be damped when connected to the highly conducting E region. Generally, the daytime E region conductance is much higher than that at night. Following the above arguments, it can be understood why our FACs reach larger amplitudes at night than during daytime (see Figures 11b1 and 11b3) although the magnetic amplitude of the events is larger during sunlit hours (see Figure 9, bottom panel), implying larger total currents in the loops. The low E region conductivity at night favors the development of narrow current structures that require high FAC densities, even for closing the fairly small total current in the loop. In this sense our observations are consistent with the conclusion of Ivarsen et al. (2019).

We are not aware of a dedicated study on daytime MSTIDs on a true global scale. Just indirect approaches, such as the ones based on electric/magnetic field fluctuations (e.g., Saito et al., 1995), or regional statistics of ionospheric parameters determined by GPS receivers (e.g., Kotake et al., 2006; Otsuka et al., 2013), exist until now. Can we be sure, without a direct comparison, that our class of morning/noon events is also related to MSTID? For checking that we determined the global distribution versus longitude, local time, and season of the events in the 04 to 14 MLT sector. The results (not shown here) exhibit very similar occurrence distributions as those shown in Figures 8–10. The much larger number of evening/nighttime SSTID events might have overridden the similar characteristics of the daytime cases. But this additional test confirms that both classes of small-scale magnetic features can be related to the same type of ionospheric irregularity. It is still puzzling why the narrow current structure appears sometimes on the poleward side and in other cases on the equatorward side of the individual current loop. And what does the difference in current configuration tell us about the dynamics and evolution of the ionospheric irregularity? Further studies are warranted, addressing these open issues.

6. Summary

Here we have presented the first detailed study on the average characteristics of small-scale magnetic fluctuations. By using 4 years (2015–2018) of data from the three Swarm satellites we have detected, with a special selection approach, a large number of events, sufficient for determining the dependences on many quantities in a statistically significant way. The main features resulting from our survey through the high-resolution magnetic field data can be summarized as follows.

1. Our small-scale (<10 km) magnetic fluctuations are deflections perpendicular to the mean field, mainly in east/west direction, without accompanying significant plasma density irregularities at Swarm altitudes. Overall, the characteristics are much the same at all three satellites. At the higher altitude of Swarm B, the event number is just a little (~10%) lower than at Swarm A&C altitude.
2. We have deduced the occurrence rate distribution of the small-scale fluctuation events. They show distinct patterns in latitude, longitude, local time, and season. They occur frequently around ±30°QD latitude, with a tendency of magnetically conjugate appearance in the Northern and Southern Hemispheres. But equatorward of ±10° QD latitude there are hardly any events detected. The largest event numbers are found in the East Asian/Australian sector. A secondary occurrence peak appears over the North Atlantic. There are practically no events observed in the region of the SAA. The largest event numbers are detected from sunset to midnight. A somewhat smaller occurrence rate is found around pre-noon hours. The seasonal dependence reveals an overwhelming number of events around June solstice in the Northern Hemisphere. During December months the smaller occurrence rate is comparable in both hemispheres. The small-scale fluctuations seem to prefer solstice summer conditions. There are very few events detected around equinoxes. All these occurrence characteristics resemble very well those of nighttime MSTIDs; therefore, we termed our events SSTIDs.

3. The magnetic fluctuations are regarded to be caused by FACs. Estimated FAC densities reveal narrow current structures (~4 km) with high current density (~3 $\mu A/m^2$). These are accompanied by comparable return currents but distributed over a wider region. The SSTID events can be sorted into two classes. The majority belongs to the evening/nighttime class lasting from about 15 to 03 MLT. The fewer remaining are the morning/noon events. In both of these classes the narrow, intense FACs are observed flowing from the Southern to the Northern Hemispheres or equally often vice versa. The intense FACs are balanced by return currents distributed over a wider sheet. FAC densities get larger and structures narrower as the events propagate toward the equator.

4. The amplitudes of magnetic fluctuations are clearly larger in sunlit regions, inferring larger total currents in the loops. But the peak FAC densities are larger in the evening-nightside sector because the horizontal scales of these FACs are smaller. This suggests that the steepening of plasma irregularities to smaller scales works better in the dark and lower conductivity environment. There seems to be a limiting process avoiding horizontal structures smaller than ~4 km. We favor the reduction in effective Pedersen conductance for very small scales as cause for it. This process could also be responsible for the dissipation of events equatorward of $\pm10°$ QD latitude.

5. The average characteristics of our nighttime SSTIDs agree very well with those published for nighttime MSTIDs. We suggest that our small structures are just a part of their evolution, when propagating equatorward. The largest FAC peaks appear near the equatorward termination latitude. Unfortunately, there are hardly any global-scale studies dedicated to daytime MSTIDs, to which we could compare our prenoon class of events. The events detected in this time sector may provide a first glance on daytime SSTID/MSTID characteristics. Related model simulations would be desired that explain the evolution of irregularities in sunlight compared to the nightside events.

References

Aoyama, T., Iyemori, T., & Nakanishi, K. (2017). Magnetic ripples observed by Swarm satellites and their enhancement during typhoon activity. *Earth, Planets and Space*, *69*, 89. https://doi.org/10.1186/s40623-017-0679-2

Arras, C. and J. Wickert (2017), Investigation of global sporadic-*E* distribution using GNSS radio occultation, Retrieved from ftp://ftp.gfz-potsdam.de/pub/home/kg/exchange/pt1mai2017/2017_0530_ARRAS.pdf

Arras, C., & Wickert, J. (2018). Estimation of ionospheric sporadic *E* intensities from GPS radio occultation measurements. *Journal of Atmospheric and Solar - Terrestrial Physics*, *171*, 60–63. https://doi.org/10.1016/j.jastp.2017.08.006

Chen, G., Zhou, C., Liu, Y., Zhao, J., Tang, Q., Wang, X., & Zhao, Z. (2019). A statistical analysis of medium-scale traveling ionospheric disturbances during 2014–2017 using the Hong Kong CORS network. *Earth, Planets and Space*, *71*(1), 52–66. https://doi.org/10.1186/s40623-019-1031-9

Forget, B., Cerisier, J.-C., Berthelier, A., & Berthelier, J.-J. (1991). Ionospheric closure of small-scale Birkeland currents. *Journal of Geophysical Research*, *96*(A2), 1843–1847. https://doi.org/10.1029/90JA02376

Heilig, B., Lühr, H., & Rother, M. (2007). Comprehensive study of ULF upstream waves observed in the topside ionosphere by CHAMP and on the ground. *Annales Geophysicae*, *25*(3), 737–754. https://doi.org/10.5194/angeo-25-737-2007

Huang, F., Dou, X., Lei, J., Lin, J., Ding, F., & Zhong, J. (2016). Statistical analysis of nighttime medium-scale traveling ionospheric disturbances using airglow images and GPS observations over central China. *Journal of Geophysical Research: Space Physics*, *121*, 8887–8899. https://doi.org/10.1002/2016JA022760

Ivarsen, M. F., Jin, Y., Spicher, A., & Clausen, L. B. N. (2019). Direct evidence for the dissipation of small-scale ionospheric plasma structures by a conductive *E* region. *Journal of Geophysical Research: Space Physics*, *124*, 2935–2942. https://doi.org/10.1029/2019JA026500

Kelley, M. C., Swartz, W. E., & Makela, J. J. (2004). Mid-latitude ionospheric fluctuation spectra due to secondary E × B instabilities. *Journal of Atmospheric and Solar-Terrestrial Physics*, *66*(17), 1559–1565. https://doi.org/10.1016/j.jastp.2004.07.004

Kil, H., & Paxton, L. J. (2017). Global distribution of nighttime medium-scale traveling ionospheric disturbances seen by Swarm satellites. *Geophysical Research Letters*, *44*, 9176–9182. https://doi.org/10.1002/2017GL074750

Kotake, N., Otsuka, Y., Tsugawa, T., Ogawa, T., & Saito, A. (2006). Climatological study of GPS total electron content variations caused by medium-scale traveling ionospheric disturbances. *Journal of Geophysical Research*, *111*, A04306. https://doi.org/10.1029/2005JA011418

Lotko, W., & Zhang, B. (2018). Alfvénic heating in the cusp ionosphere-thermosphere. *Journal of Geophysical Research: Space Physics*, *123*, 10,368–10,383. https://doi.org/10.1029/2018JA025990

Lühr, H., Park, J., Ritter, P., & Liu, H. (2012). In-situ CHAMP observation of ionosphere-thermosphere coupling. *Space Science Reviews*, *168*(1-4), 237–260. https://doi.org/10.1007/s11214-011-9798-4

Lühr, H., Warnecke, J. F., & Rother, M. K. A. (1996). An algorithm for estimating field-aligned currents from single spacecraft magnetic field measurements: A diagnostic tool applied to Freja satellite data. *IEEE Transactions on Geoscience and Remote Sensing*, *34*(6), 1369–1376. https://doi.org/10.1109/36.544560

Nakanishi, K., Iyemori, T., Taira, K., & Lühr, H. (2014). Global and frequent appearance of small spatial scale field-aligned currents possibly driven by the lower atmospheric phenomena as observed by the CHAMP satellite in middle and low latitudes. *Earth, Planets and Space*, *66*(1), 1–16. https://doi.org/10.1186/1880-5981-66-40

Otsuka, Y., Suzuki, K., Nakagawa, S., Nishioka, M., Shiokawa, K., & Tsugawa, T. (2013). GPS observations of medium-scale traveling ionospheric disturbances over Europe. *Annales Geophysicae*, *31*, 163–172. https://doi.org/10.5194/angeo-31-163-2013

Park, J., Lühr, H., Kervalishvili, G., Rauberg, J., Michaelis, I., Stolle, C., & Kwak, Y. S. (2015). Nighttime magnetic field fluctuations in the topside ionosphere at midlatitudes and their relation to medium-scale traveling ionospheric disturbances: The spatial structure and scale sizes. *Journal of Geophysical Research: Space Physics*, *120*, 6818–6830. https://doi.org/10.1002/2015JA021315

Park, J., Lühr, H., & Rauberg, J. (2013). Global characteristics of Pc1 magnetic pulsations during solar cycle 23 deduced from CHAMP data. *Annales Geophysicae*, *31*(9), 1507–1520. https://doi.org/10.5194/angeo-31-1507-2013

Park, J., Lühr, H., Stolle, C., Rodriguez-Zuluaga, J., Knudsen, D. J., Burchill, J. K., & Kwak, Y. S. (2016). Statistical survey of nighttime midlatitude magnetic fluctuations: Their source location and Poynting flux as derived from the Swarm constellation. *Journal of Geophysical Research: Space Physics*, *121*, 11,235–11,248. https://doi.org/10.1002/2016JA023408

Park, J., Lühr, H., Stolle, C., Rother, M., Min, K. W., Chung, J.-K., et al. (2009). Magnetic signatures of medium-scale traveling ionospheric disturbances as observed by CHAMP. *Journal of Geophysical Research*, *114*, A03307. https://doi.org/10.1029/2008JA013792

Park, J., Lühr, H., Stolle, C., Rother, M., Min, K. W., & Michaelis, I. (2009). The characteristics of field-aligned currents associated with equatorial plasma bubbles as observed by the CHAMP satellite. *Annales Geophysicae*, *27*(7), 2685–2697. https://doi.org/10.5194/angeo-27-2685-2009

Park, J., Stolle, C., Lühr, H., Rother, M., Su, S. Y., Min, K. W., & Lee, J. J. (2008). Magnetic signatures and conjugate features of low-latitude plasma blobs as observed by the CHAMP satellite. *Journal of Geophysical Research*, *113*, A09313. https://doi.org/10.1029/2008JA013211

Richmond, A. D. (1995). Ionospheric electrodynamics using magnetic apex coordinates. *Journal of Geomagnetism and Geoelectricity*, *47*(2), 191–212. https://doi.org/10.5636/jgg.47.191

Rodríguez-Zuluaga, J., & Stolle, C. (2019). Interhemispheric field-aligned currents at the edges of equatorial plasma depletions. *Scientific Reports*, *9*(1), 1–8. https://doi.org/10.1038/s41598-018-37955-z

Rother, M., Schlegel, K., & Lühr, H. (2007). CHAMP observation of intense kilometer-scale field-aligned currents, evidence for an ionospheric Alfvén resonator. *Annales Geophysicae*, *25*(7), 1603–1615. https://doi.org/10.5194/angeo-25-1603-2007

Saito, A., Iyemori, T., Blomberg, L. G., Yamamoto, M., & Takeda, M. (1998). Conjugate observations of the mid-latitude electric field fluctuations with the MU radar and the Freja satellite. *Journal of Atmospheric and Solar-Terrestrial Physics*, *60*(1), 129–140. https://doi.org/10.1016/S1364-6826(97)00094-1

Saito, A., Iyemori, T., Sugiura, M., Maynard, N. C., Aggson, T. L., Brace, L. H., et al. (1995). Conjugate occurrence of the electric field fluctuations in the nighttime midlatitude ionosphere. *Journal of Geophysical Research*, *100*(A11), 21,439–21,451. https://doi.org/10.1029/95ja01505

Shiokawa, K., Otsuka, Y., Ihara, C., Ogawa, T., & Rich, F. J. (2003). Ground and satellite observations of nighttime medium-scale traveling ionospheric disturbance at midlatitude. *Journal of Geophysical Research*, *108*(A4), 1145. https://doi.org/10.1029/2002JA009639

Sivakandan, M., Chakrabarty, D., Ramkumar, T. K., Guharay, A., Taori, A., & Parihar, N. (2019). Evidence for deep ingression of the midlatitude MSTID into as low as ~3.5° magnetic latitude. *Journal of Geophysical Research: Space Physics*, *124*, 749–764. https://doi.org/10.1029/2018JA026103

Stolle, C., Lühr, H., Rother, M., & Balasis, G. (2006). Magnetic signatures of equatorial spread *F* as observed by the CHAMP satellite. *Journal of Geophysical Research*, *111*, A02304. https://doi.org/10.1029/2005JA011184

Swartz, W. E., Kelley, M. C., & Aponte, N. (2009). *E*- and *F*-region coupling between an intense sporadic e layer and a mesoscale traveling ionospheric disturbance. *Annales Geophysicae*, *27*(6), 2475–2482. https://doi.org/10.5194/angeo-27-2475-2009

Tsugawa, T., Kotake, N., Otsuka, Y., & Saito, A. (2007). Medium-scale traveling ionospheric disturbances observed by GPS receiver network in Japan: A short review. *GPS Solutions*, *11*(2), 139–144. https://doi.org/10.1007/s10291-006-0045-5

Yokoyama, T., Hysell, D. L., Otsuka, Y., & Yamamoto, M. (2009). Three-dimensional simulation of the coupled Perkins and Es-layer instabilities in the nighttime midlatitude ionosphere. *Journal of Geophysical Research*, *114*, A03308. https://doi.org/10.1029/2008JA013789

Yokoyama, T., & Stolle, C. (2016). Low and midlatitude ionospheric plasma density irregularities and their effects on geomagnetic field. *Space Science Reviews*, *206*(1–4), 495–519. https://doi.org/10.1007/s11214-016-0295-7

Yu, S., Xiao, Z., Aa, E., Hao, Y., & Zhang, D. (2016). Observational investigation of the possible correlation between medium-scale TIDs and mid-latitude spread *F*. *Advances in Space Research*, *58*(3), 349–357. https://doi.org/10.1016/j.asr.2016.05.002